Transient simulation of an atmospheric boundary layer flow past a heliostat using the Scale-Adaptive Simulation turbulence model

Poulain P.[a], Craig K.J.[a,*], Meyer J.P.[a]

[a]Department of Mechanical and Aeronautical Engineering
University of Pretoria, Pretoria 0002, South Africa

Abstract

Heliostat fields are exposed to changing climatic conditions as they are mostly erected in open environments where the wind naturally features a high unsteadiness at low altitude due to the ground effects. Much of the computational fluid dynamics (CFD) content in the open literature is focused on Reynolds-averaged-Navier-Stokes (RANS) simulations, which can only predict mean loads. This paper considers an isolated heliostat in worst-case orientation. The drag force is numerically modelled by means of a Scale-Resolving Simulation (SRS) in ANSYS v19. This paper firstly deals with two different methods that generate perturbations at the inlet boundary: the spectral synthesizer and the vortex method. In an empty domain, an atmospheric boundary layer (ABL) profile is modelled based on a wind tunnel experiment. Secondly, the wind tunnel test of a single heliostat model in upright orientation is replicated, aiming to model the mean and peak drag forces. Applicable for highly separated flows, the Scale-Adaptive Simulation (SAS) turbulence model is employed as it is computationally more affordable than a Detached Eddy Simulation (DES) approach. The latter would require a higher grid resolution and a reduced time step size. The SAS showed little but acceptable decay of the inlet profiles whilst achieving lateral homogeneity. The mean and root-mean-square error of the drag force signal showed a deviation with the experiment of 0.04 % and 5.8 %, respectively, whereas the error on the peak drag forces was around 18 %, possibly mostly due to the under-prediction of the turbulent integral length scale at the model location.

Nomenclature

Δ	Cell edge length	m
ϵ	Turbulence dissipation rate	m^2/s^3
κ	von Kármán constant	
μ_t	Eddy viscosity	$Pa \cdot s$
Ω	Vorticity magnitude	s^{-1}
ω	Specific dissipation rate	s^{-1}
Ω_{CV}	Cell volume	m^3
$\overline{U}$	Time average of U	m/s
ρ	Air density	kg/m^3
σ	Standard deviation	
c	Heliostat chord length	m
C_{Fx}	Drag force coefficient	
C_{MHy}	Overturning moment coefficient	
C_{My}	Base overturning moment coefficient	
Co	Courant number	
f	Normalised frequency	
f_s	Sampling frequency	Hz
F_x	Drag force	N
HCL	Height of centreline of heliostat	m
I_x	Longitudinal turbulence intensity	
k	Turbulence kinetic energy	m^2/s^2
L_t	Turbulence integral length scale	m
L_u^x	Longitudinal integral length scale of turbulence	m
L_u^x	Longitudinal integral length scale	m
M_y	Base overturning moment	$N.m$
MH_y	Overturning moment	$N.m$
n	Frequency	Hz
$RMSE$	Root-mean-square error	
S	Strain rate magnitude	s^{-1}
S_u	Power spectral density of the longitudinal fluctuating velocity	$m^2 \cdot s^{-2} \cdot Hz^{-1}$
U	Local velocity magnitude	m/s
u'_x	Longitudinal fluctuating velocity	m/s
U_x	Longitudinal velocity	m/s
u_*	Friction velocity	m/s
y^+	Non-dimensional wall distance	
z_0	Surface roughness length	m

*Corresponding author: Tel.: +27- 12- 420- 3515; E-mail address: ken.craig@up.ac.za

Keywords: computational fluid dynamics (CFD); Scale-Adaptive Simulation (SAS); atmospheric boundary layer (ABL); heliostat; turbulence power spectrum

1. Introduction

1.1. Background

Due to an increase in greenhouse gas emissions, combined with declining reserves of fossil fuels, there is a global determination towards investing in renewable energies in order to increase their representation in the energy mix. Although one can raise the issue of intermittency for some of them, forecasting methods and models can be improved so that the supply and demand are adjusted accordingly (Zhang et al., 2020). There is also a considerable drive for the study and design of small-scale power generation technologies as they can be integrated into urban areas (Longo et al., 2020). Photovoltaic technology has shown the possibility of harvesting solar energy and is providing hope for previously aborted projects in concentrating solar power (CSP). However, a cheaper storage capacity and a greater dispatchability offers great advantages for CSP. The total installed costs of CSP plants could decrease by more than one-third between 2015 and 2025 (IRENA, 2016). A higher storage capacity will increase a CSP plant capacity factor and lower its capital cost (IRENA, 2020). Namely, in 2018 and 2019, the median capital cost of a CSP project with a storage capacity between 4 and 8 hours was 5,914 USD/kW versus 4,976 USD/kW for over 8 hours. The four types of CSP plants are presented in Figure 1. The linear Fresnel and the parabolic dish power plants are smaller-scale technologies. The electricity generation lies between 0.1 and 0.2 MW hour per year per square metre of reflective area (National Renewable Energy Laboratory, 2017). The capacity does generally not exceed 30 MW. Parabolic trough and solar tower power plants generally generate over 0.3 MW hour per year per square metre of reflective area. They are larger-scale projects as they are designed to feature capacities over 50 MW.

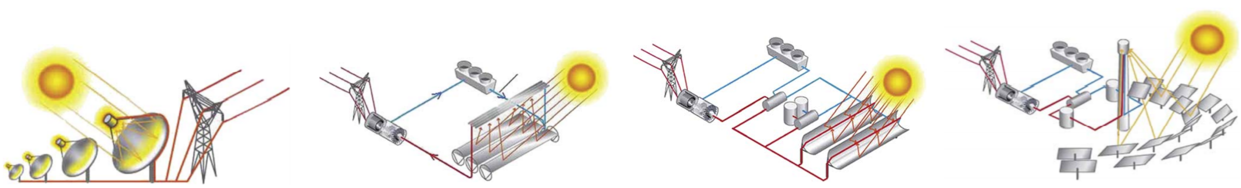

(a) Parabolic dish (b) Linear Fresnel (c) Parabolic trough (d) Solar tower

Figure 1: Schematics of the various CSP plants (Blanco and Santigosa, 2016)

There has been a growing interest in the solar tower technology since there is a global increase in plant efficiency relative to parabolic troughs. In 2015, the levelised cost of energy (LCOE) of both technologies was ranging from 0.15 to 0.19 USD/kWh with a slighlty more advantaging reference value for the solar towers (0.161 USD/kWh versus 0.165 USD/kWh for troughs). In 2025, both reference values should drop to 0.104 USD/kWh for trough plants versus 0.091 USD/kWh for solar tower plants (IRENA, 2016). The latter offer greater concentration ratios, therefore taking the heat transfer fluid to a higher temperature, which in return increases the storage efficiency. Molten salt used for storage purposes can also be utilised as the working fluid. Higher temperatures allow the use of more efficient turbines. All of these make for higher capacity factors for the solar tower power plants. Another advantage is that the reflectors can be implanted on uneven ground and moderately hilly terrains. A detailed comparison of the various characteristics of the different CSP technologies has been reported by IRENA (2012) in the form of a table. In most cases, the profitability of a power plant is improved by increasing the efficiency of some of its sub-systems. However, regarding the solar tower technology, one can greatly diminish the total capital cost of a plant by building the heliostat field at a lower cost. Indeed, every single unit has its own drive mechanism system and must withstand the wind loads to which it is subjected throughout the lifetime of the power plant. As depicted on Figure 2, the heliostat field of a solar tower power station can comprise several hundreds of thousands of units and represents around 40 % of its total capital cost (Pidaparthi, 2017).

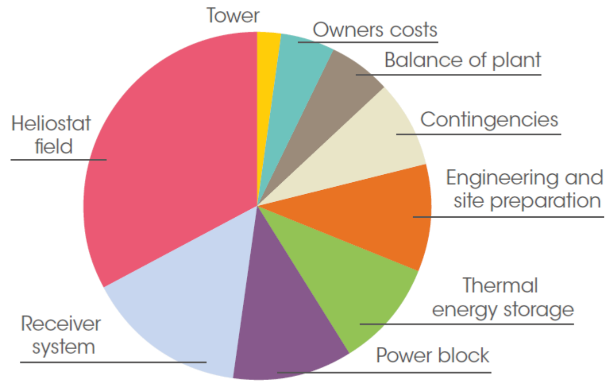

Figure 2: Cost breakdown for a CSP tower plant in South Africa (IRENA, 2012)

Although wind tunnel tests are preferred for heliostat design, CFD provides valuable information for the design and optimisation of a heliostat structure (e.g. Pfahl et al. (2011b),Emes et al. (2017), Paetzold et al. (2014), Marais et al. (2015)). It delivers a good representation of the flow field all around the model whereas wind tunnel tests are limited to measured datasets. The number of CFD studies that cover wind loading on heliostats remains low, however. These studies are mostly tied to RANS simulations. Besides, this is not sufficiently rigorous since RANS models assume the turbulence to be isotropic which is mostly not the case in reality. Moreover, due to time-averaging, such simulations do not enable the computation of peak loads which are required for heliostat design at operational wind conditions. Wind loading within the atmospheric boundary layer (ABL) is strongly time-dependent and this has to appear in the characteristics of the flow. The aim of the study is to replicate a wind tunnel test of Peterka et al. (1986) with ANSYS Fluent v19 using a SRS turbulence model solving in transient mode.

1.2. Literature review

The solar tower technology projects date as far back as the early 1980s (Breeze, 2019). Although wind tunnel tests are generally undertaken in the final stages of the structural design in order to assess the strength of a prototype that is submitted to wind loading, they are also used to investigate possible innovations. Numerous wind tunnel tests have been carried out over the past four decades and one can find results and findings in the literature. Peterka et al. performed extensive wind tunnel experiments for the CSP field. They gathered data and provided results in several comprehensive reports (Peterka et al., 1986, 1987b, 1988, 1990) and scientific publications (Peterka et al., 1987a, 1989). They compiled their tests and research and issued guidances for the structural design of heliostats and parabolic dish collectors (Peterka and Derickson, 1992). Pfahl et al. also carried out several wind tunnel experiments aiming at improving heliostat design and decreasing the manufactural costs (Pfahl et al., 2011a,b, 2014, Pfahl, 2018). Pfahl (2014) listed the concepts for the cost reduction of heliostats, detailed their advantages and drawbacks and contributed to a review summarising the state of the art around heliostats (Pfahl et al., 2017). On a techno-economic aspect, Blackmon (2013, 2014) made parametric investigations leading to safety factors and fatigue life assessments as well as heliostat optimal reflective area estimations, whilst Emes et al. (2015, 2020) worked on correlations between ABL characteristics and heliostat structural design. Liu et al. (2014) studied the influence of wind fences around the heliostat field on wind loads. This has also been partly investigated by Peterka et al. (1986, 1987b, 1988) along with the impact of the collectors field density. Peterka et al. (1987b, 1988) realised that the collectors are highly sensitive to the gustiness of the approaching wind. Emes et al. (2017, 2018) examined this phenomenon for isolated and tandem heliostats in the stow position. One can also find several full-scale studies and validation data in the literature (Sment and Ho, 2014, Vásquez-Arango et al., 2015, Zang et al., 2012, Griffith et al., 2011, Rebolo et al., 2011, Gong et al., 2015). Peterka et al. (1987b) has studied the shape of the mirror (circular versus square) while Pfahl et al. (2011a) focused on the impact of the heliostat aspect ratio. Both studies used wind tunnel tests only. Assuming a gust factor for the ratio of peak to mean loads has been found to underestimate the peak loads, especially in stow position. The peak coefficients have been shown to be dependent on the turbulence intensity and integral length scales in the approaching ABL. This is discussed by Peterka and Derickson (1992), Pfahl (2018), Emes et al. (2019) and

Jafari et al. (2019), based on wind tunnel measurements. Since the design strength of a collector should be rather directly based on the peak wind loads (Peterka et al., 1987b), the objective of the researchers is to build a CFD model that can compute the peak loads with acceptable accuracy.

Although the accuracy of CFD RANS simulations is often not satisfactory enough in a dynamic loading framework, Huss et al. (2011) showed that the change in the wind loads with both elevation and azimuth angles matches with trends given by experimental results. Besides, it can provide meaningful information for a given trend in the experimental data. For instance, Pfahl et al. (2011b) measured a 20 % increase of the hinge moment in its worst case orientation for a heliostat with a wide central gap compared to a solid heliostat. Through CFD analyses, they realised that the leeward pressure distribution is greatly influenced by the gap. Another advantage of CFD is the possibility to explore a wide range of structural designs and variables before fabricating a model that will undergo wind tunnel tests. Marais et al. (2015) and Marais (2016) developed a numerical method that optimises a heliostat aspect ratio based on wind loading moments endured by the drive mechanisms. Wu et al. (2010) showed numerically and experimentally that small gaps between heliostat facets do not have an impact on the wind loading.

In this study,the researchers aim to model the air flow past a heliostat. The collector is oriented so as to be perpendicular to the incoming mean flow, acting as a bluff body in the maximum drag orientation. The resulting vortex shedding phenomenon excites the structural components of the heliostat, affects the pressure distribution on the leeward side of the collector and may have a considerable impact on the accuracy of the solution (Chen and Chiou, 1998). Unfortunately, RANS models fail to resolve the most energy-containing turbulent structures and represent most of the interactions between the vorticies of different scales (Fröhlich and von Terzi, 2008). Most CFD studies that address wind loading in CSP are done using RANS simulations (Christo, 2012, Zemler et al., 2013), Large Eddy Simulation (LES) (Boddupalli et al., 2017, Hachicha et al., 2013, 2014) or hybrid RANS/LES methods such as SAS (Paetzold et al., 2014, 2015, 2016), Stress-Blended Eddy Simulation (Wolmarans and Craig, 2019) or Detached Eddy Simulation (Poulain et al., 2016b). One can combine transient simulations with a modal analysis in order to assess the dynamic wind loading of a structure. Fluid-structure interaction studies have previously been carried out for a heliostat collector (Vásquez-Arango et al., 2017, Wolmarans and Craig, 2019) in an attempt to link the resolved flow field with the structural response. Although LES greatly improves the accuracy of a model, the computational cost of the simulation increases as well. Indeed, the mesh has to be fine enough so that most of the turbulence energy spectrum is resolved which can become problematic in the near-wall area where both the cell aspect ratio and the y^+ have to be close to 1. Such a stringent condition will affect the total computational cost further since a smaller time step has to be set. Therefore, the challenge is to achieve acceptable accuracy in the results with a minimum computational time. For this reason, this study focuses on the ability of the SAS turbulence model to compute the drag force on a heliostat collector submitted to ABL flow. The advantage it has over any RANS model is that it can substantially resolve the turbulent fluctuations (Fröhlich and von Terzi, 2008) for a much lower computational time compared to solving with LES. It has previously shown good agreement with experimental values and can sometimes perform better than RANS and hybrid RANS/LES models (Egorov et al., 2010, Maliska et al., 2012, Zheng et al., 2016). This case, being a flow past a bluff body, falls in the range of application of this model (Menter, 2012).

1.3. Layout

In the first place, this paper will introduce the SAS turbulence model used in this work and will detail its specificities and advantages for transient simulations. The next section focuses on the ABL and the equations developed to model its fully-developed profile. It will also give a view on how one can characterise the turbulence energy content of the flow with the help of the power spectral density (PSD). The researchers have conducted two CFD simulations for this study. The first one verifies whether one can reproduce appropriate wind conditions in the modelled wind tunnel. The second one aims model the drag force on a heliostat in its upright orientation, which is the worst case in terms of wind loading caused by the drag force. Both the CFD simulations will be detailed and the results will shed light on data sampling frequency and solution convergence for the simulation. The researchers also present flow characteristics and compare the drag force against experimental values before making conclusions.

2. Methodology

2.1. Scale-Adaptive Simulation turbulence model

The concept of SAS has been introduced with the aim of relieving turbulence models of their grid dependency for the resolution of turbulent structures (Menter et al., 2003). The SAS model is based on an exact transport equation for the turbulence length scale developed by Rotta (1972). In Rotta's $k-kL$ model, the influence of the second derivative of the velocity field appearing in the source term of the scale equation is cancelled under the isotropic turbulence assumption. However, aiming to resolve the bigger turbulent structures of a non-homogeneous flow, this assumption is unsatisfactory (Menter and Egorov, 2006). The second derivative velocity allows the model to adjust its length scale to those structures already resolved in the flow (Menter, 2012), hence the use of the denomination "scale-adaptive". In ANSYS Fluent, the momentum equations are transposed to the $k-\omega$ formulation (Equations 1 and 2). The additional Q_{SAS} term (Equation 3) includes the von Karman length scale, L_{vK}, which does not appear in any standard RANS model (Equation 4). The model originally failed to dissipate the smallest-scale eddies (Egorov and Menter, 2008). Therefore, a limiter has been designed based on the Wall-Adapting Local Eddy-viscosity model in order to achieve high wave number damping. A lower limit on the calculation of the eddy viscosity, μ_t, is enforced (Menter and Egorov, 2010). This limiter is proportional to the mesh cell size, Δ, which is derived from the cubic root of the control volume size, Ω_{CV} (Equation 4). The values of the model constants are presented in Table 1 and their calibration can be found in Menter and Egorov (2010). F_1 refers to the blending function defined for the baseline $k-\omega$ model (ANSYS, 2019).

$$\frac{\partial \rho k}{\partial t} + \frac{\partial}{\partial x_i}(\rho U_i k) = G_k - \rho c_\mu k\omega + \frac{\partial}{\partial x_j}\left[\left(\mu + \frac{\mu_t}{\sigma_k}\right)\frac{\partial k}{\partial x_j}\right] \quad \text{with} \quad G_k = \mu_t S^2 \tag{1}$$

$$\frac{\partial \rho \omega}{\partial t} + \frac{\partial}{\partial x_i}(\rho U_i \omega) = \alpha\frac{\omega}{k}G_k - \rho\beta\omega^2 + Q_{SAS} + \frac{\partial}{\partial x_i}\left[\left(\mu + \frac{\mu_t}{\sigma_\omega}\right)\frac{\partial \omega}{\partial x_j}\right] + (1-F_1)\frac{2\rho}{\sigma_{\omega,2}}\frac{1}{\omega}\frac{\partial k}{\partial x_j}\frac{\partial \omega}{\partial x_j} \tag{2}$$

$$Q_{SAS} = \max\left[\rho\eta_2\kappa S^2\left(\frac{L}{L_{vK}}\right)^2 - C\frac{2\rho k}{\sigma_\phi}\max\left(\frac{1}{\omega^2}\frac{\partial \omega}{\partial x_j}\frac{\partial \omega}{\partial x_j}, \frac{1}{k^2}\frac{\partial k}{\partial x_j}\frac{\partial k}{\partial x_j}\right), 0\right] \tag{3}$$

$$L = \frac{\sqrt{k}}{c_\mu^{1/4}\omega}, \quad L_{vK} = \max\left(\kappa\left|\frac{U'}{U''}\right|, C_S\sqrt{\frac{\kappa\eta_2}{\frac{\beta}{c_\mu}-\alpha}}\cdot\Delta\right) \quad \text{with} \quad \Delta = \Omega_{CV}^{1/3} \tag{4}$$

$$\text{where} \quad U' = S = \sqrt{2\cdot S_{ij}S_{ij}} \quad \text{with} \quad S_{ij} = \frac{1}{2}\left(\frac{\partial U_i}{\partial x_j} + \frac{\partial U_j}{\partial x_i}\right) \quad \text{and} \quad U'' = \sqrt{\frac{\partial^2 U_i}{\partial x_k^2}\frac{\partial^2 U_i}{\partial x_j^2}}$$

c_μ	σ_k	β	σ_ω	$\sigma_{\omega,2}$	η_2	C	σ_ϕ	C_S	α
0.09	2.0	0.072	2.0	1.168	3.51	2	2/3	0.11	1

Table 1: SAS model constants

2.2. Atmospheric boundary layer and inlet boundary conditions

2.2.1. General equations

The ABL to which the heliostats are subjected is not uniform and features lower velocities closer to the ground but higher fluctuations translate into a higher turbulence intensity. Ideally, to generate such a profile, one should model the presence of ground elements upstream of the heliostat model. However, this would require an extension of the upstream part of the domain as well as a fine mesh around the turbulence-generating elements (e.g. spires and surface roughness elements), all of which resulting in a much higher number of cells, therefore increasing the computation time. In order to address this issue, the use of fully-developed profiles generated at the inlet boundary of the domain is recommended. Richards and Hoxey (1993) derived a set of equations (equations 5, 6 and 7) for the $k-\epsilon$ turbulence model based on three main assumptions in order to achieve a horizontally homogeneous ABL profile: no vertical velocity, constant pressure and constant shear stress. The ABL friction velocity, u_*, can be calculated using reference values for height and velocity:

$$u(z) = \frac{u_*}{\kappa} \ln\left(\frac{z+z_0}{z_0}\right) \quad \text{with} \quad u_* = \frac{\kappa u_{ref}}{\ln\left(\frac{z_{ref}+z_0}{z_0}\right)} \tag{5}$$

$$k = \frac{u_*^2}{\sqrt{c_\mu}} \tag{6}$$

$$\epsilon(z) = \frac{u_*^3}{k\,(z+z_0)} \tag{7}$$

The surface roughness length, z_0, represents the height of the ground roughness elements. One can play around with this parameter to alter the inlet profiles. In fact, an increase will globally result in a lower mean velocity but a higher turbulence intensity, I, which represents the fluctuations within the velocity field. For RANS simulations, it is calculated with Equation 8. It has been experimentally shown that results are highly sensitive to the turbulence intensity level of the incoming velocity profile (Peterka et al., 1987b). For that matter, the researchers aimed to obtain a fairly good match of the turbulence intensity inlet profile generated in the CFD model with the experimental one that they have extracted from Peterka et al. (1986).

$$I = \frac{\sqrt{\frac{2}{3}k}}{U} \quad \text{where U is the local velocity magnitude} \tag{8}$$

2.2.2. Mean inlet boundary conditions

In the CFD model, the velocity inlet boundary condition generates the profiles by means of a User-Defined Function (UDF) that contains the system of equations developed for an ABL profile presented in the previous section. Unfortunately, Peterka et al. (1986) do not mention the reference velocity used for the elaboration of their profiles. However, they measured a 40.0 ft/s wind speed at a full-scale height of 10 m during the run (number 99 in their Appendix B) that the researchers aim to reproduce. Knowing their reference height ($z_{ref} = 44.7$ in at model scale), the researchers deduced their reference velocity, $U_{ref} = 16.26$ m/s. A surface roughness length of $z_0 = 0.0008$ m was chosen to match both the experimental turbulence intensity and velocity profiles (figures 3 and 4). After applying the scale factor of the experiment which is 1/60, the full-scale value for the CFD simulation corresponds to an open farmland with few trees and buildings (Burton et al., 2001). This corresponds with values for a typical environment surrounding a CSP plant.

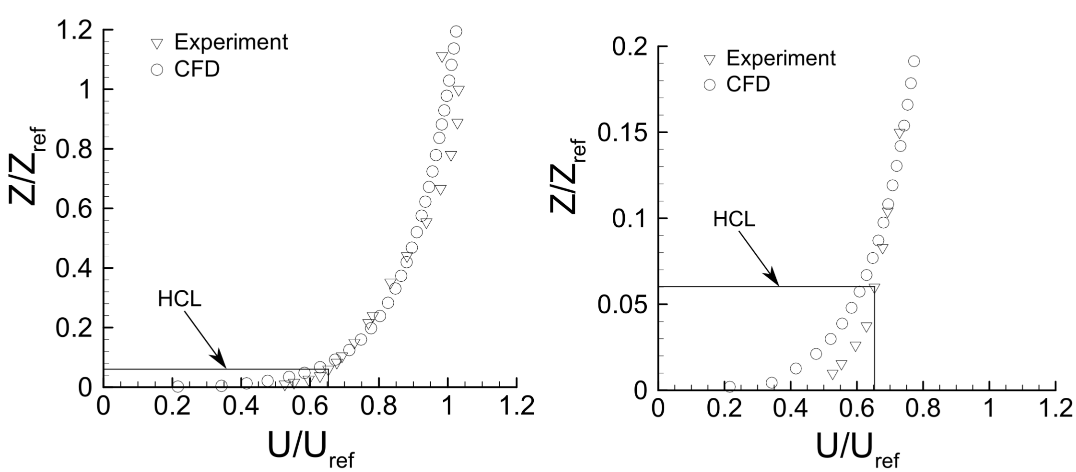

Figure 3: Velocity profile of ABL - Experimental (Peterka et al., 1986) versus CFD, global (left) and zoomed view (right)

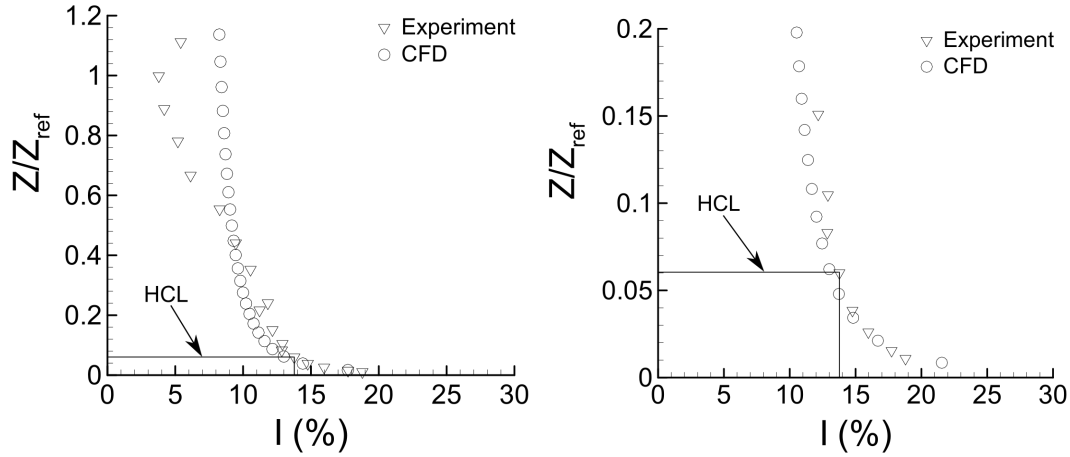

Figure 4: Turbulence intensity profile of ABL - Experimental (Peterka et al., 1986) versus CFD, global (left) and zoomed view (right)

Although the turbulence intensity is not exactly matched at the height of the centreline of the heliostat (HCL) (13 % in the CFD versus 13.7 % as the digitised experimental value), it has been decided to proceed with these profiles because increasing the surface roughness length would alter them. Indeed, close to the ground, the velocity profile would present lower values and a higher gradient, whereas the turbulence intensity profile would feature higher values and a higher gradient as well.

2.2.3. Fluctuating inlet boundary conditions

ANSYS Fluent v19 gives four methods for the generation of fluctuating velocity components at the velocity inlet boundary: no perturbations, spectral synthesizer, vortex method and synthetic turbulence generator. In the current work, the focus will be on the spectral synthesizer and the vortex method. The "no perturbations" option is not suitable for ABL flows due to the high levels of turbulence at stake, whereas the synthetic turbulence generator method will be investigated at a later stage.

The spectral synthesizer method is based on the random flow generation technique developed by Kraichnan (1970) and later modified by Smirnov et al. (2001). This method produces fluctuating velocity components. They are computed from the summation of 100 Fourier harmonics and the result is a divergence-free velocity field (ANSYS, 2019). The implementation of the vortex method in ANSYS Fluent v19 derives from the work of Sergent (2002). Vortices are injected through the inlet plane and advected into the domain.

Figures 5a and 5c present the differences between both these methods in terms of the vortices distribution on the inlet face and their vorticity magnitude. Monitoring this quantity in a plane that goes throughout the domain, one can see that the spectal synthesizer shows an important decrease streamwise that the vortex method seems to somewhat overcome (figures 5b and 5d).

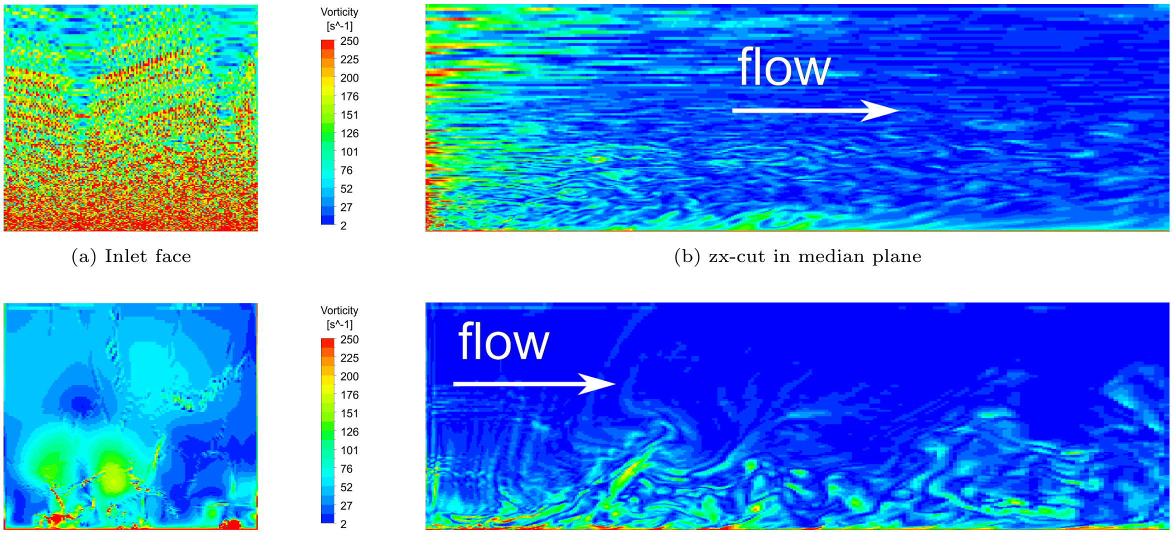

(a) Inlet face

(b) zx-cut in median plane

(c) Inlet face

(d) zx-cut in median plane

Figure 5: Vorticity magnitude contours with (a,b) illustrating the spectral synthesizer and (c,d) illustrating the vortex method

The vortical structures are displayed in Figure 6 using the iso-surfaces of the Q-criterion, which is defined as $\frac{1}{2}\left(\Omega^2 - S^2\right)$ with Ω being the vorticity magnitude and S being the strain rate magnitude. This criterion delineates flow regions where the vorticity magnitude is greater than the magnitude of the rate of strain. As can be seen on Figure 6, there is a great difference in the turbulence kinetic energy level carried by the vortices generated at the inlet and the value specified as a boundary condition ($k = 2.81\,\mathrm{m}^2/\mathrm{s}^2$ from Equation 6). Such a discrepancy could be corrected by using a turbulent kinetic energy profile at the inlet boundary as proposed by Gorlé et al. (2010) and Lauriks et al. (2021). This will be done in future work as it is more realistic for ABL flows. Downstream of the inlet, the turbulent kinetic energy of the vortical structures globally increases as they travel into the domain and interact with one another. The vortices generated by the spectral synthesizer expand in a streamwise direction which is not realistic within a non-uniform velocity profile. Moreover, most of the turbulent structures start to dissipate after the first third of the domain. It has therefore been decided to set aside the spectral synthesizer method and pursue with the vortex method regarding the inlet boundary condition of both the CFD models to follow. The vortex method also features streamwise velocity fluctuations with a simplified linear kinematic model based on the vorticity field derived at the inlet boundary. The size of each vortex derives from a turbulent mixing length hypothesis and the known mean profiles of the turbulent kinetic energy and dissipation rate (Mathey et al., 2006).

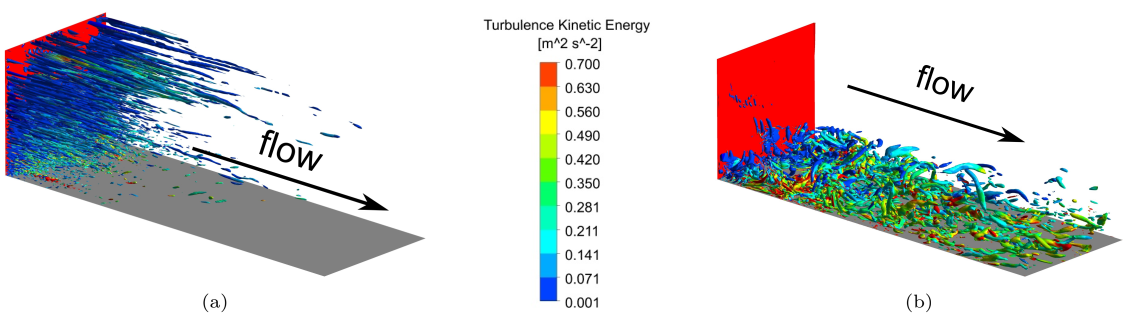

(a)

(b)

Figure 6: Iso-surface of Q-criterion ($2,000\,\mathrm{s}^{-2}$) coloured by the turbulence kinetic energy with (a) the spectral synthesizer and (b) the vortex method

2.2.4. Longitudinal turbulence power spectrum

With transient simulations, it becomes possible to observe the frequency content of the velocity fluctuations and verify that the energy injected into the flow is in accordance with what has been observed in the experiment and in full-scale measurements. This is done through the visualisation of the PSD of the velocity fluctuations. Several models have been developed in the past century for the ABL's PSD and one can find the expressions presented hereafter in Balendra et al. (2002) for equations 9 and 12 and in Simiu and Scanlan (1996) for equations 10, 11 and 13. Most often, the reduced spectrum of the longitudinal velocity fluctuations is considered and plotted against the Monin coordinate $f = nz/U(z)$, n being the frequency. In Equation 9, the longitudinal turbulence integral length scale, L_u^x, represents the size of the eddies in the streamwise direction. Peterka et al. (1986) compared their spectrum against one developed by Harris through full-scale measurements. They presented it in the form of a normalised spectrum plotted against a normalised frequency as it incorporates the variations of a spectrum due to differences in measurement height and/or velocity.

$$\text{von Kármán}: \quad \frac{nS_u(z,n)}{u_*^2} = \frac{4\frac{nL_u^x}{U}}{\left[1 + 70.8\left(\frac{nL_u^x}{U}\right)^2\right]^{5/6}} \tag{9}$$

$$\text{Davenport}: \quad \frac{nS_u(z,n)}{u_*^2} = 4.0\frac{x^2}{(1+x^2)^{4/3}} \quad \text{where} \quad x = \frac{1200n}{U(10)} \tag{10}$$

$$\text{Harris}: \quad \frac{nS_u(n)}{u_*^2} = 4.0\frac{x}{(2+x^2)^{5/6}} \quad \text{where} \quad x = \frac{1800n}{U(10)} \tag{11}$$

$$\text{Kaimal}: \quad \frac{nS_u(z,n)}{u_*^2} = \frac{100f}{3(1+50f)^{5/3}} \tag{12}$$

$$\text{Simiu}: \quad \frac{nS_u(z,n)}{u_*^2} = \frac{200f}{(1+50f)^{5/3}} \tag{13}$$

2.3. Numerical method

2.3.1. Geometry and boundary conditions

For both an empty wind tunnel and one containing the heliostat model, the computational domain expands to 6 m in the streamwise direction (x ranges from 0 to 6 m) and the cross-section is $2.05 \times 1.83\,\text{m}^2$ (z ranges from 0 to 1.83 m and y from -1.025 to 1.025 m). In order to replicate the wind tunnel test of Peterka et al. (1986), the side and top walls are set to a zero-shear stress boundary condition. This has the effect of nullifying the normal velocity gradient at the boundary, forcing the flow in a streamwise direction. To address the decay of the inlet profiles noticed in previous work (Poulain et al., 2016a), a retarding shear stress of $\tau_w = \rho u_*^2$ is applied on the ground wall for the precursor RANS simulation (Figure 7). The exit of the domain is given a pressure outlet boundary condition. The researchers will subsequently present a CFD model of an isolated heliostat with no thickness in upright orientation. As shown on Figure 7, the heliostat geometry used is highly similar to the one tested by Peterka et al. (1986). The three panels have equal dimensions and are spaced with a 5 mm gap. The diameters of both the pylon and the torque tube have not been reported and have been made 3 mm. The torque tube length of the experimental heliostat model seems to be slightly greater than the total width of the heliostat. However, this should only have a negligible impact on the flow distribution, if any. Another unknown dimension is the distance between the reflective area and the torque tube which is set to 3 mm in the CFD model.

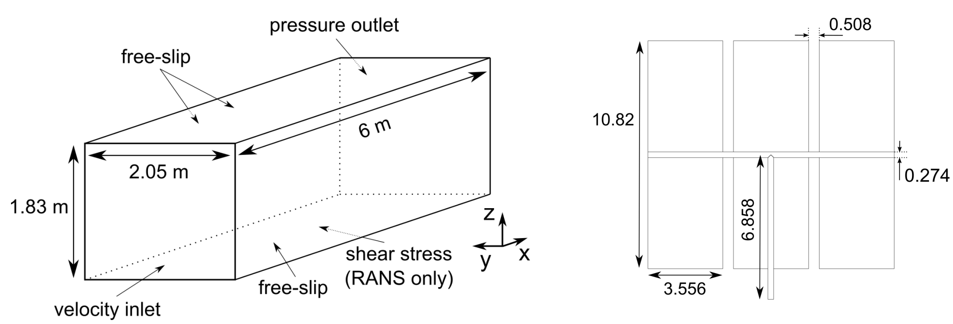

Figure 7: Computational domain and heliostat model (dimensions in cm)

2.3.2. Mesh

The empty domain has been meshed with 6.2 million hexahedrons, which form a structured grid. Our second model containing the heliostat in upright orientation has a grid that is mostly structured with 23.4 million cells. Only the vicinity of the hinge has been meshed with tetrahedrons. The mesh count could have been sensibly higher if the researchers had modelled the heliostat thickness. Not reported in Peterka et al. (1986), the latter is 3 mm in Peterka et al. (1987b). For instance, using five cells across the heliostat thickness to model the flow separation that occurs would make a cell length of 0.6 mm in this area. Choosing a smaller mesh size here would inevitably reverberate on the rest of the grid which would greatly increase the total mesh count. This highlights the challenge of achieving a good mesh resolution with a minimal computational time. The mesh becomes finer around all the edges of the heliostat so that it can capture the vortex shedding phenomenon and feature the shear layer with a high definition (Figure 8). The refined sections in the middle of a panel are due to the presence of the torque tube or the pylon. Regarding the wall treatment in ANSYS Fluent v19, the turbulence models based on the specific dissipation rate, ω, are independent of the near-wall y^+ resolution. More specifically, it is done by blending the viscous sublayer and the logarithmic layer formulations based on the y^+. Being derived from the $k-\omega$ turbulence model, the SAS model features this versatility. With the help of mesh interfaces, several levels of coarsening occur in the three directions of the grid (Figure 9). At every mesh interface, for three cell edges on the fine side there are two corresponding cell edges on the coarse side. Nonetheless, there is no mesh interface in the wake region in order to avoid numerical artefacts within this area. Contrary to the isolated heliostat model, the empty wind tunnel model has been carried out with the use of a conformal mesh.

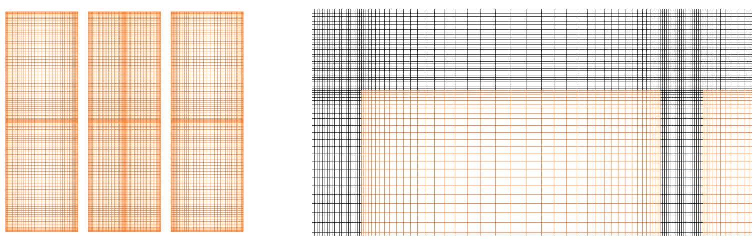

Figure 8: Surface mesh of the heliostat panels (orange) and around (black)

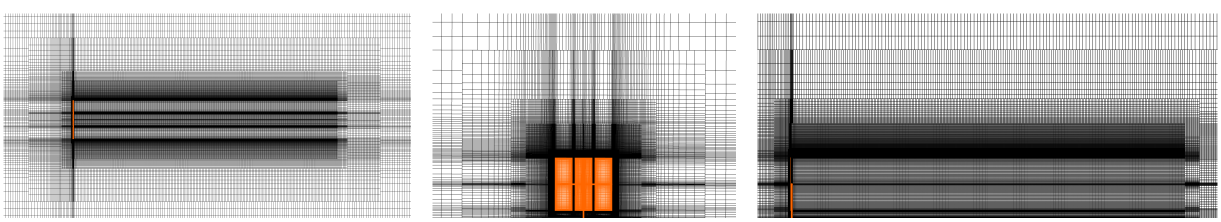

Figure 9: Mesh interfaces in planes xy (left), yz (centre) and zx (right)

2.3.3. Grid convergence study

For the meshing of the heliostat CFD model, the focus was on the gaps and the torque tube and pylon diameter as they have smaller dimensions. Three different meshes have been used for a RANS simulation with the realizable $k-\epsilon$ model. The coarsest one was composed of 3.3 million cells. The second and third meshes resulted from the refinement of the former by a factor of 2.6 in the three directions to obtain 8.6 and then 22.3 million cells. The drag force exerted on the collector computed by CFD simulations on these meshes was compared with the result given by the fine grid (Figure 10). Through calculations of grid convergence indices with a safety factor of 1.25 and the order of convergence for the drag force, the researchers verified that they were in the range of asymptotic convergence as they obtained a factor of 0.974, thus ensuring mesh independence.

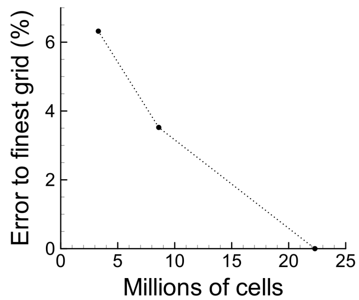

Figure 10: Comparison of the error between the coarser grids and the finest grid on the drag force computed with CFD RANS simulations

2.3.4. Mesh size assessment

Performing a precursor steady-state RANS simulation before switching to a transient SRS model is strongly recommended (Gerasimov, 2016). Not only will it give a proper initial state of the flow when switching to the transient mode, but it will also provide information about the relative fineness of the mesh as required when using an SRS model. This has been done for both the CFD models. It is advised to resolve 80 % of the turbulence content in order to obtain a solution that is accurate enough (Pope, 2000). This means that the domain should be meshed so as to have approximately five cells across the integral length scale of turbulence, L_t, computed from the following equation (Gerasimov, 2016):

$$L_t = \frac{k^{\frac{3}{2}}}{\epsilon} \tag{14}$$

With Δ the mesh size as defined in Equation 4, displaying the contours of the ratio L_t/Δ with the range clipped from 0 to 5 highlights whether and where the mesh needs to be refined. For the empty wind tunnel model, except for the near-wall area, part of the viscous sublayer, the mesh was fine enough as it abides by the requirement of five cells across the integral length scale of turbulence. Regarding the heliostat model, a few zones would need to be refined. On Figure 11, one can see the iso-surface of 5 for the ratio L_t/Δ. This iso-surface encapsulates regions of even lower values. Similar to the empty wind tunnel model, the heliostat near-wall area features small length scales for the dissipation of turbulence. The flow separation induced by the pylon in the clearance gap presents a low resolution, as does the whole region located a few centimetres behind the heliostat gaps. This is due to the interaction of the wake with the air flowing through the clearance gap and the proximity of the model. This combination causes a high dissipation rate in this region. However, with the shear layer generated by the edges around the model being the dominant factor for the drag force caused on the collector, the choice was made to perform the transient simulation with this mesh.

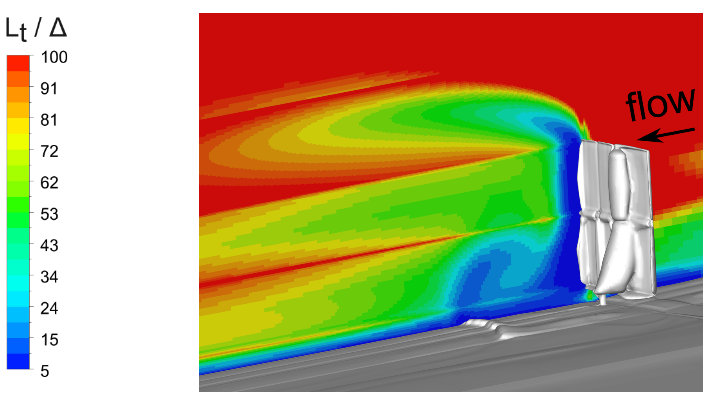

Figure 11: Iso-surface of $L_t/\Delta = 5$ (grey) and contours of this ratio on a zx-plane going through the centre of a gap

2.3.5. Time step

One can also assess an appropriate time step size, Δt, for the transient simulation. Ideally, one tries to keep the Courant number, Co, below 1 in order to satisfy the Courant-Friedrichs-Lewy condition. Hence the creation of the following custom field function, where U is the local velocity magnitude given by the RANS precursor simulation:

$$\Delta t = \frac{Co\,\Delta}{U} \quad \text{with} \quad Co = 1 \tag{15}$$

For the empty wind tunnel configuration, the researchers obtained a minimum value of 1.5×10^{-4} s in the whole computational domain and conservatively chose a time step of $\Delta t = 10^{-4}$ s for the transient simulation. With the presence of the heliostat model, the grid becomes much finer, therefore this minimum value drops to 1.2×10^{-5} s. It has been decided not to set a lower time step size than the former requirement and to keep the same value for the heliostat model simulation in order to avoid a large increase of the total computation time. This is acceptable given that an iterative implicit scheme is used for time discretisation (bounded-second order). Moreover, the areas that require a smaller time step are located where the turbulence will mostly be modelled (Figure 12). The model and wake nearby regions also depict a lower time step requirement due to a fine mesh within a free-stream velocity zone.

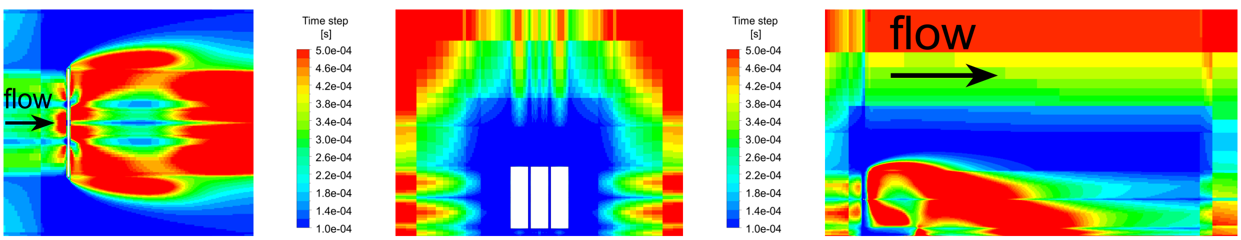

(a) xy-view at HCL (b) yz-plane at the panels (c) zx-view at mid-gap location

Figure 12: Contours of the time step estimation around the heliostat model and in its wake

3. Results

3.1. Empty wind tunnel

3.1.1. Solution convergence

The empty wind tunnel model simulated 5 seconds of flow time in about 26 hours (including the time for data export) at a Centre for High Performance Computing (CHPC), using 10 nodes (Intel Xeon E5-2690 v3, 2.60 GHz) of 24 cores each. A brief run of the delayed DES turbulence model on the same grid has shown to be 35 % slower. The monitoring of the solution convergence was done from data collection at point surfaces created at z = HCL for several streamwise locations. The three components of the velocity vector were exported at every time step and statistics were computed. Using the Reynolds decomposition, the fluctuating velocity components can be determined by subtracting the velocities time-average from their signal (Equation 16). The longitudinal turbulence intensity, I_x, is calculated from the standard deviation of the longitudinal fluctuating velocity (Equation 17). The longitudinal turbulence power spectrum, $S_u(n)$, was derived from the magnitude squared of the Fast Fourier Transform of the longitudinal fluctuating velocity.

$$U_{x,y,z}(t) = \overline{U_{x,y,z}} + u'_{x,y,z}(t) \tag{16}$$

$$I_x = \frac{\sigma_{u'_x}}{\overline{U}} \tag{17}$$

Van der Hoven (1957) made a power spectrum analysis of the longitudinal wind speed. The higher frequencies peak, caused by the turbulence within the ABL (Cook, 1986), covers a period between 5 s and 5 min (Vásquez-Arango et al., 2017) and reaches its maximum for a period of about 72 s. In other words, this is the period at which the most energy-containing structures occur. Regarding the CFD model, there could be some uncertainty as to whether or when convergence has been reached. Although one may consider the longitudinal velocity time average to be converged from 50 s of the simulated time, the longitudinal turbulence intensity keeps increasing for the monitor point placed at $x = 1$ m and keeps decreasing for all the other monitor points (Figure 13). The steep increase that occurs at the inlet 70 s into the simulation (Figure 13b) is due to the generation of a vortex near the monitor point. Another method for convergence considerations could be the monitoring of a spatial average made in the spanwise direction, in other words for a given streamwise location and height, averaging all the values in the lateral direction. By construction, the fluctuating components of the velocity should have a time average of 0 m/s (Figure 14a). This is however practically impossible and a tolerance has to apply. An idea would be to evaluate the absolute value of the ratio $\left|\overline{u'_x}/\overline{U_x}\right|$. In this case, this ratio drops below 1 % after 70 s of simulated time and below 0.1 % slightly before 150 s (Figure 14b).

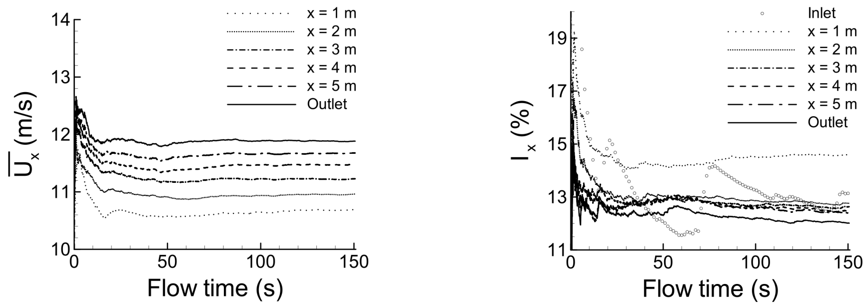

(a) (b)

Figure 13: Evolution of (a) the longitudinal velocity time average and (b) the longitudinal turbulence intensity at z = HCL for the seven 1 m-spaced monitor points

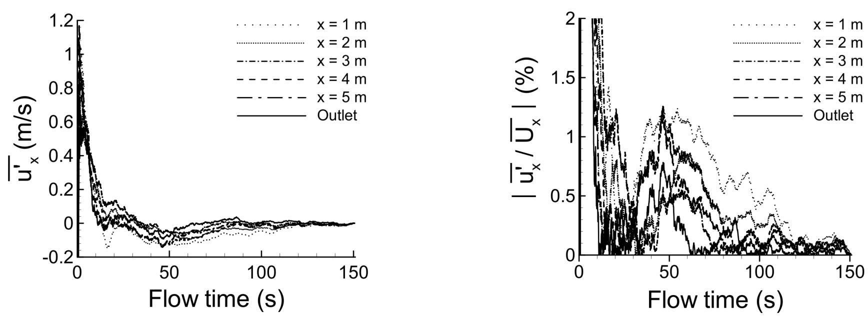

(a) (b)

Figure 14: Evolution of (a) the longitudinal fluctuating velocity time average and (b) its ratio with the longitudinal velocity time average at z = HCL for several streamwise locations

3.1.2. Profiles and longitudinal turbulence power spectrum

As the flow travels through the domain, there is a decrease of the turbulence intensity at HCL from 2 m onwards conjugated to an increase of the longitudinal velocity time average (Figure 15). One can see that this occurs over the whole profile for both quantities (figures 16 and 17). The sudden rise taking place in the turbulence intensity profile between $Z/Z_{ref} = 0.2$ and $Z/Z_{ref} = 0.5$ for $x = 1$ m and $x = 2$ m results from vortices generated at the inlet about these heights but dissipated under the mean flow characteristics. As the turbulence intensity is a driving parameter for heliostat wind loading (Peterka et al., 1987b), it has been decided to place the heliostat model 1.5 m away from the inlet boundary, allowing for the development of the vortical structures generated by the vortex method, while remaining close to the experimental turbulence intensity value at HCL (14 %). Another possibility would be to generate profiles with a higher turbulence intensity than the experimental targeted value in order to account for the decay. The model could then be placed about 4 m from the inlet, in the area where the turbulence intensity profile is nearly horizontally homogeneous. However, this would mean extending the domain size, which would lead to an increase in computational time. In this study, because $Z_{HCL}/Z_{ref} = 0.0604$, the heliostat model will not experience the aforementioned sudden rise in turbulence intensity. As evoked in 2.2.3, it would be of interest to see the evolution of the turbulence characteristics and profiles with a turbulent kinetic energy varying with height at the inlet.

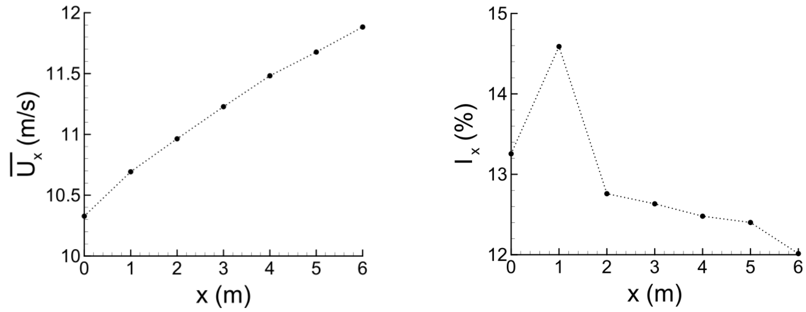

(a) (b)

Figure 15: Streamwise evolution at $z =$ HCL of (a) the longitudinal velocity and (b) the longitudinal turbulence intensity

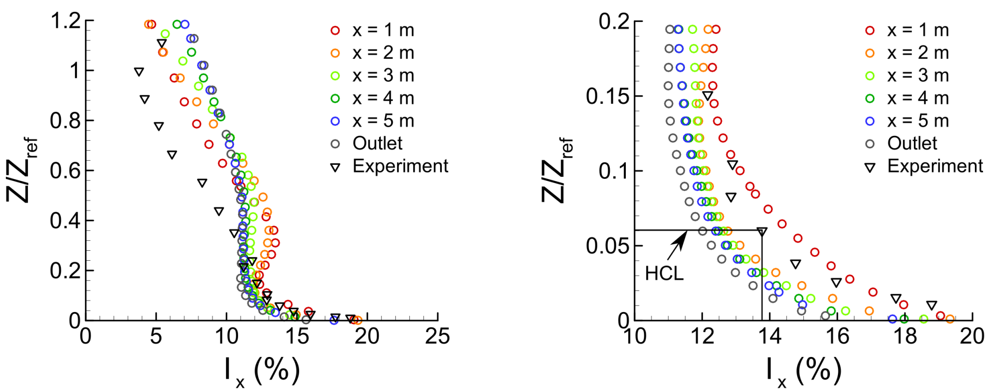

Figure 16: Streamwise evolution of the turbulence intensity profile versus experiment (Peterka et al., 1986), global (left) and zoomed view (right)

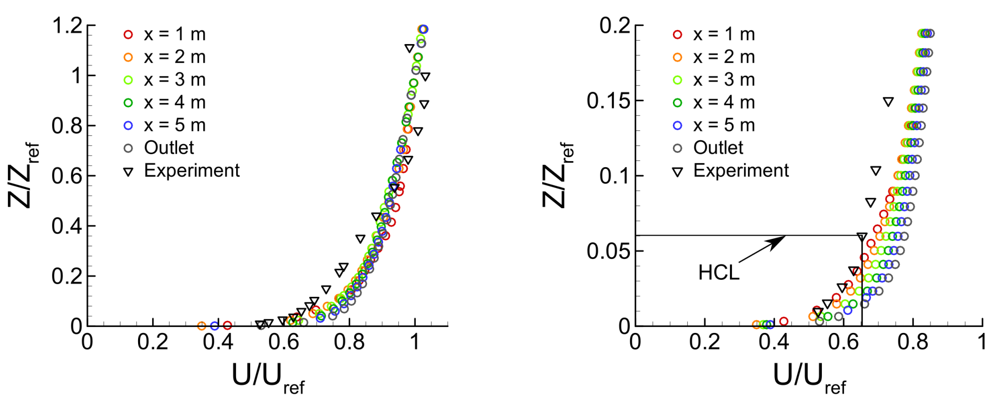

Figure 17: Mean velocity profile at several streamwise locations versus experiment (Peterka et al., 1986), global (left) and zoomed view (right)

The spanwise variations of the mean longitudinal velocity and longitudinal turbulence intensity have been investigated with the computation of the variables presented in Equation 18. The values of $y = \pm 0.05842$ m correspond to the lateral coordinates of the edges of the heliostat model. The profiles at the locations $x = 1$

and 2 m have been exported. Although the previous graphs showed a decay of the inlet profiles, lateral homogeneity is achieved with a deviation relative to the centreline values that is between $\pm 1\,\%$ for the mean longitudinal velocity and between $\pm 5\,\%$ for the longitudinal turbulence intensity (Figure 18).

$$\frac{\overline{U_x(x,y,z)} - \overline{U_x(x,0,z)}}{\overline{U_x(x,0,z)}} \quad \text{and} \quad \frac{I_x(x,y,z) - I_x(x,0,z)}{I_x(x,0,z)} \tag{18}$$

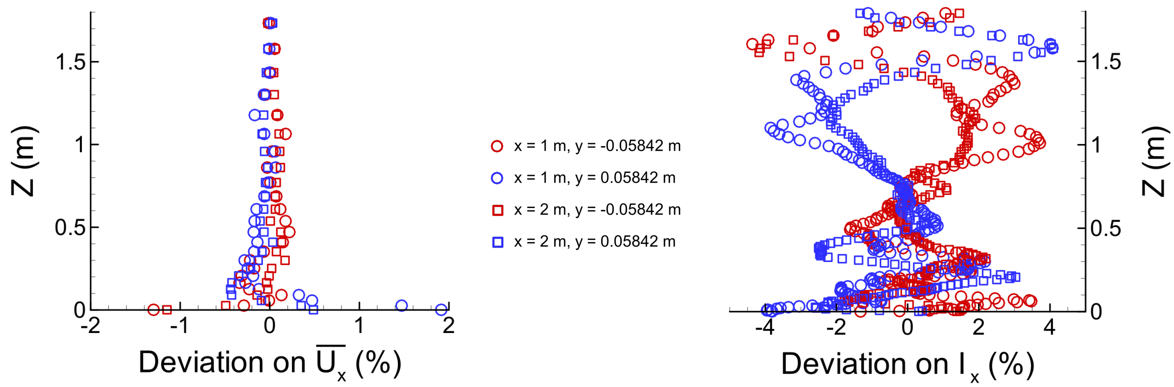

Figure 18: Deviation of the mean longitudinal velocity (left) and the longitudinal turbulence intensity (right) profiles relative to the centreline profile ($y = 0\,\mathrm{m}$)

The longitudinal turbulence power spectrum has been computed for every point surface and compared with the experimental one (Figure 19). In the lower frequency range (f roughly between 0.001 and 0.03), the further downstream the monitor point is located, the bigger the eddies. However, this trend reverses past the frequency for which the amplitude is maximum meaning that vortices of a given size occur more frequently as one travels upstream. Various total sampled times have been explored to determine the minimum required time of the simulation for a converged solution. The simulation has been stopped after 150 s of flow time has been modelled. For total sampled times of 20 and 30 s, although one can see an overprediction of the turbulent length scales of the eddies in the lower frequency range, for frequencies greater than 0.01 there is no major difference in comparison with the longitudinal turbulence spectrum when the total sampled time matches the total duration of the simulation (Figure 20).

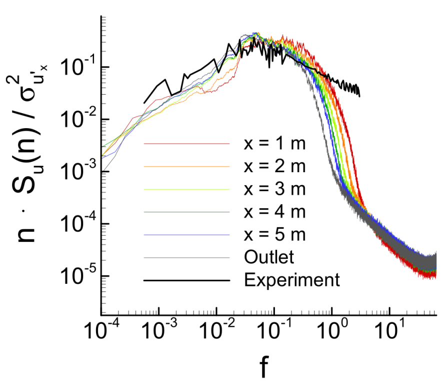

Figure 19: Streamwise evolution of the longitudinal turbulence spectrum at HCL versus experiment (Peterka et al., 1986)

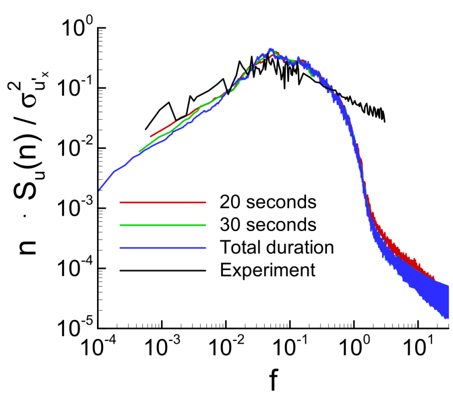

Figure 20: Variations of the longitudinal turbulence spectrum with the total sampled time at HCL for $x = 3\,\mathrm{m}$

The profile of the longitudinal integral length scale of turbulence, L_u^x, has been computed for the seven streamwise locations (Figure 21) by integrating the autocorrelation function of the longitudinal fluctuating velocity over the total sampled time. One can see that the vortices generated at the inlet are not fully developed within the first half of the domain. The integral length scale of the experiment was reported as being “four times larger than the characteristic length of the heliostat model” (Peterka et al., 1986). Based on the heliostat chord length, this leads to a value of 0.4328 m. In this regard, placing the model 1.5 m downstream of the inlet boundary might not be appropriate and a distance of 5 m could have been considered (Figure 22). This is in line with the longitudinal turbulence spectrum being better approximated in the frequency range around the peak (Figure 19). A linear interpolation gives a value of 0.2575 m at $x = 1.5$ m which makes an error of 40.5 % with the experimental value aforementioned.

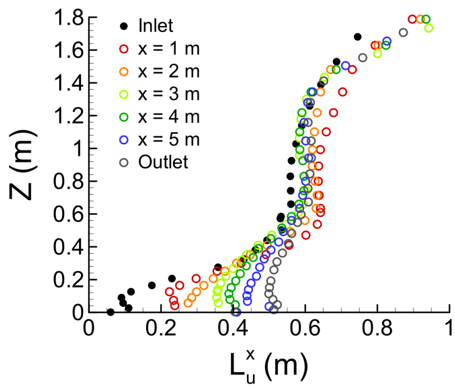

Figure 21: Streamwise evolution of the longitudinal turbulent integral length scale profile at the centreline ($y = 0$ m)

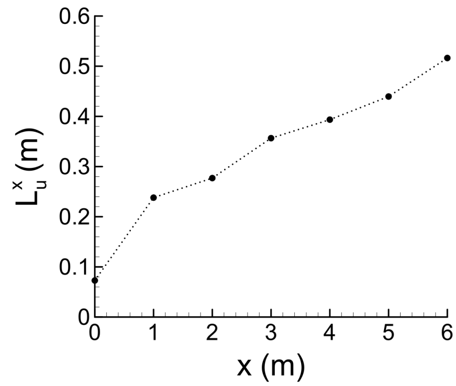

Figure 22: Streamwise evolution at $z =$ HCL of the longitudinal integral length scale of turbulence

3.1.3. Data sampling frequency

The large number of time steps required for the convergence of the simulation implied the generation of a copious amount of data files, therefore increasing the total computational time, the space disk usage, as well as the post-processing time required. For these simulations, datasets were exported at every time step, i.e. with a sampling frequency of $f_s = 10,000$ Hz. However, as depicted in Figure 23, reducing the quantity of information collected by a factor of 100 would not have had a negative effect on the results. This is important to consider given that exporting data slows down a simulation and also increases the computing time during the post-processing step.

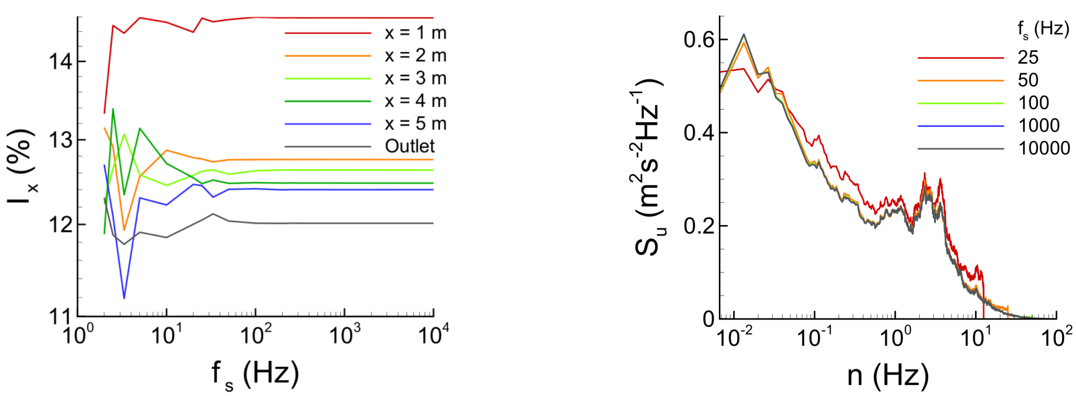

(a)

(b)

Figure 23: Influence of the sampling frequency on (a) the longitudinal turbulence intensity and (b) the PSD of the longitudinal fluctuating velocity at $x = 3$ m (both at HCL)

3.2. Heliostat model

In the experiment, the peak loads refer to “the largest and smallest values recorded during a time of [...] 32 seconds model scale” Peterka et al. (1986). As it was unsure how much simulation time was required to achieve statistical convergence, the transient simulations were run at the Centre for High Performance Computing (CHPC) in Cape Town, South Africa. For the empty wind tunnel model, 5 seconds of flow time could be run in about 17 hours using 10 nodes (Intel Xeon E5-2690 v3, 2.60 GHz) of 24 cores each. Regarding the heliostat model, 25 seconds could be simulated within one month using the same resources and a total of 46 seconds was sampled. In Figure 24, one can see the presence of vortical structures in the incoming flow, as well as the vortex-shedding phenomenon caused by the collector. A lower Q-criterion value displays more vortices, but a higher one shows the turbulent structures that contain the most energy.

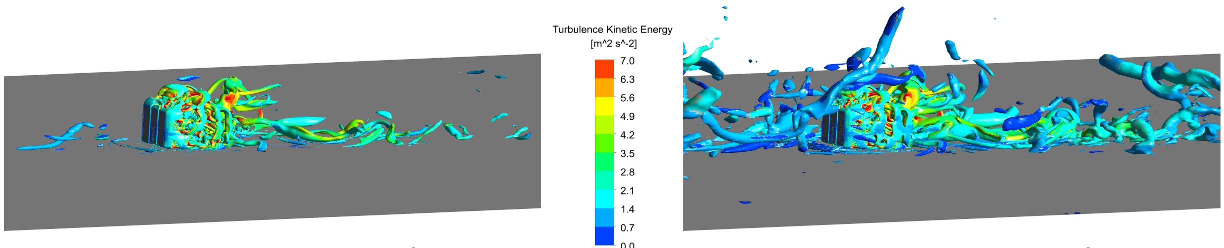

(a) $\mathrm{Q-criterion} = 100,000\,\mathrm{s}^{-2}$ (b) $\mathrm{Q-criterion} = 20,000\,\mathrm{s}^{-2}$

Figure 24: Iso-surfaces of Q-criterion coloured by the turbulence kinetic energy

Because of time-averaged velocity variations upstream of the model and the fact that the distance between the measuring probe and the heliostat model was not reported in Peterka et al. (1986), it was decided to monitor the drag force, F_x, rather than its non-dimensional coefficient, C_{Fx} (Equation 19). The peak and mean drag forces of the wind tunnel experiment can be deduced based on the reference values. Note that the reference area includes the gaps between the panels. Therefore, a drag force coefficient of 1.26 corresponds to a force of 1.45 N and the minimum and maximum drag force coefficients measured at 0.60 and 2.56, respectively, give a minimum of 0.69 N and a maximum of 2.95 N. A sample of the drag force signal and its running time average is depicted in Figure 25 and the results of the CFD simulation are presented in Table 2. The SAS turbulence model shows that it can accurately predict the mean drag force on the heliostat. However, there is a non-negligible imprecision with regard to the peak drag forces, although the accuracy of the experiment "was about 5 to 10 percent or better of the maximum value recorded" (Peterka et al., 1986). The amplitude of the signal should indeed be greater and this is in line with the lower root-mean-square error (RMSE) obtained with the CFD simulation. Nevertheless, an error of about 18 % is found for the peak values and one can investigate on introducing a safety factor for the peak loads modelled with the SAS turbulence model. It is noteworthy that, although the thickness of the collector was not modelled, this did not have a negative impact on the mean drag force.

$$F_x = \frac{1}{2}\rho A_{ref} U_{10\mathrm{m}}^2 C_{Fx} \quad \text{with} \quad A_{ref} = 126.43\,\mathrm{cm}^2 \quad \text{and} \quad U_{10\mathrm{m}} = 12.192\,\mathrm{m/s} \tag{19}$$

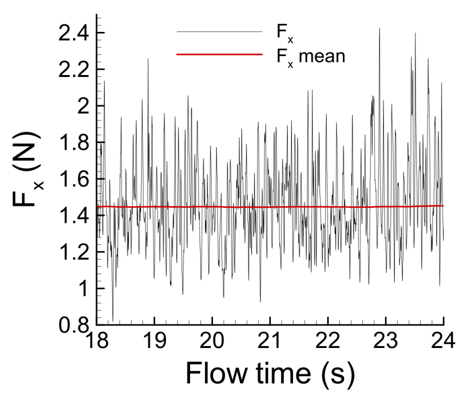

Figure 25: Sample of the evolution of the drag force and its time average

F_x (N)	Mean	RMSE	Min	Max
Peterka et al. (1986)	1.45	0.24	0.69	2.95
CFD	1.4509	0.2251	0.8176	2.4260
Error	0.04 %	5.8 %	18.4 %	17.7 %

Table 2: Results for the drag force from the CFD SAS compared against the experiment

The overturning moment at the hinge, MH_y, has also been modelled. The base moment will, however, be compared since it also reaches a maximum under the heliostat orientation presented. The combination of equations 19, 20 and 21 (Peterka et al., 1987b) leads to Equation 22, given that the reference length is equal to the heliostat chord length. Table 3 shows an error of 8 % for the base overturning moment relatively to the experiment.

$$MH_y = \frac{1}{2}\rho A_{ref} L_{ref} U_{10\mathrm{m}}^2 C_{MHy} \quad \text{with} \quad L_{ref} = 10.82\,\mathrm{cm} \tag{20}$$

$$C_{My} = C_{MHy} + C_{Fx}\frac{HCL}{c} \tag{21}$$

$$M_y = MH_y + F_x \times HCL \tag{22}$$

	M_y mean (N.m)
Peterka et al. (1986)	0.11
CFD	0.0994
Error	8.1 %

Table 3: Results for the mean base overturning moment from the CFD SAS compared against the experiment

One can also question whether the pylon and torque tube have to be represented, given their insignificant share in the results (Table 4). They may, however, play a role in the flow separation in the clearance gap and in the pressure distribution on the back of the panels. If this is not verified, excluding both of them from the geometry would contribute to a gain of time during the meshing step, as well as reduced computational cost.

Elements	Panels	Torque tube	Pylon	Hinge
Ratio to F_x	99.7 %	0.15 %	0.19 %	4×10^{-5} %

Table 4: Contribution of the various heliostat components towards the mean drag force

4. Conclusion

This study focused on the possibility of modelling an ABL flow with a reasonable computational cost. It showed the ability of the SAS turbulence model to reproduce an ABL profile with limited horizontal inhomogeneity, unlike RANS models applied in their standard form. The modelling of the transient mean and peak drag forces exerted on a heliostat in an upright orientation was assessed and comparisons were made with the wind tunnel test of Peterka et al. (1986). Good agreement was found regarding the mean and the RMSE values. However, the error on the peak drag forces remains in the range of 18 %. This could be linked to the longitudinal turbulence spectrum being under-predicted in the low frequency range.

Another important result is that it does not seem necessary to model the thickness of the heliostat in this orientation, which has the direct effect of decreasing the computational cost considerably as the mesh size around the collector would be of the order of 0.1 mm otherwise. However, the modeling of the peak loads for other orientations, such as the ones that produce a maximum lift force and hinge overturning moment (panels inclined by 30 ° relative to the horizontal plane) and a maximum azimuthal moment (upright heliostat, but turned so as to form a 65 ° angle with the incoming flow), should be undertaken. The necessity of modelling the torque tube and the pylon is questioned since their absence would allow for bigger mesh cells in the related areas.

Further work will be done with the SAS turbulence model as it leads to computationally affordable CFD simulations. However, the horizontal homogeneity issue depicted in this study needs to be adressed. The focus will be set on the influence of the streamwise domain length on the evolution of the longitudinal turbulence intensity and power spectrum as well as the integral length scale. The impact of having a turbulent kinetic energy profile at the inlet boundary will also be investigated in this regard. It could indeed alleviate the important streamwise variations seen for the various profiles. Finally, the synthetic turbulence generator will be tested and compared against the vortex method utilised in this study.

5. Acknowledgement

The authors would like to thank the University of Pretoria, as well as the South African National Research Foundation (DSI-NRF Solar Spoke) for their support. They would additionally like to acknowledge the CHPC in Cape Town, South Africa, that made these simulations achievable.

References

T. Balendra, D. Shah, K. Tey, and S. Kong. Evaluation of flow characteristics in the NUS-HDB wind tunnel. Journal of Wind Engineering and Industrial Aerodynamics, 90(6):675–688, 2002.

J. B. Blackmon. Parametric determination of heliostat minimum cost per unit area. Solar Energy, 97: 342–349, 2013.

J. B. Blackmon. Heliostat drive unit design considerations – Site wind load effects on projected fatigue life and safety factor. Solar energy, 105:170–180, 2014.

M. Blanco and L. R. Santigosa. Advances in concentrating solar thermal research and technology. Woodhead Publishing, 2016.

N. Boddupalli, V. Goenka, and L. Chandra. Fluid flow analysis behind heliostat using LES and RANS: A step towards optimized field design in desert regions. In AIP Conference Proceedings, volume 1850. AIP Publishing LLC, 2017.

P. Breeze. Power Generation Technologies. Newnes, 3rd edition, 2019.

A. Burton, N. Jenkins, D. Sharpe, and E. Bossanyi. Wind Energy Handbook. Wiley, 2001.

J. Chen and C.-C. Chiou. Experimental investigation of a parallel vortex-plate interaction. Journal of Fluids and Structures, 12(3):295 – 314, 1998.

F. C. Christo. Numerical modelling of wind and dust patterns around a full-scale paraboloidal solar dish. Renewable Energy, 39(1):356–366, 2012.

N. J. Cook. Designers guide to wind loading of building structures. Part 1. 1986.

Y. Egorov and F. R. Menter. Development and application of SST-SAS turbulence model in the DESIDER project. In Advances in Hybrid RANS-LES Modelling, pages 261–270. Springer, 2008.

Y. Egorov, F. R. Menter, R. Lechner, and D. Cokljat. The Scale-Adaptive Simulation method for unsteady turbulent flow predictions. Part 2: Application to complex flows. Flow, Turbulence and Combustion, 85 (1):139–165, 2010.

M. Emes, M. Arjomandi, F. Ghanadi, and R. Kelso. Effect of turbulence characteristics in the atmospheric surface layer on the peak wind loads on heliostats in stow position. Solar Energy, 157(08):284–297, 2017.

M. Emes, F. Ghanadi, M. Arjomandi, and R. Kelso. Investigation of peak wind loads on tandem heliostats in stow position. Renewable Energy, 121(03):548–558, 2018.

M. J. Emes, M. Arjomandi, and G. J. Nathan. Effect of heliostat design wind speed on the levelised cost of electricity from concentrating solar thermal power tower plants. Solar Energy, 115:441–451, 2015.

M. J. Emes, A. Jafari, F. Ghanadi, and M. Arjomandi. Hinge and overturning moments due to unsteady heliostat pressure distributions in a turbulent atmospheric boundary layer. Solar Energy, 193:604–617, 2019.

M. J. Emes, A. Jafari, J. Coventry, and M. Arjomandi. The influence of atmospheric boundary layer turbulence on the design wind loads and cost of heliostats. Solar Energy, 207:796–812, 2020.

J. Fröhlich and D. von Terzi. Hybrid LES/RANS methods for the simulation of turbulent flows. Progress in Aerospace Sciences, 44(07):349–377, 2008.

G. Gerasimov. Quick guide to setting up LES-type simulations, 2016.

B. Gong, Z. F. Wanga, C. C. Zanga, and Z. N. Li. Model updating and structure optimization of heliostats based on vibration measurements. Energy Procedia, 69, 2015.

C. Gorlé, J. van Beeck, and P. Rambaud. Dispersion in the wake of a rectangular building: Validation of two Reynolds-Averaged Navier-Stokes modelling approaches. Boundary-layer meteorology, 137(1):115–133, 2010.

D. Griffith, A. Moya, C. Ho, and P. Hunter. Structural dynamics testing and analysis for design evaluation and monitoring of heliostats. Journal of Solar Energy Engineering, 137, January 2011.

A. Hachicha, I. Rodríguez, J. Castro, and A. Oliva. Numerical simulation of wind flow around a parabolic trough solar collector. Applied Energy, 107:426 – 437, 2013.

A. Hachicha, I. Rodríguez, O. Lehmkuhl, and A. Oliva. On the CFD&HT of the flow around a parabolic trough solar collector under real working conditions. Energy Procedia, 49:1379–1390, 2014.

S. Huss, Y. D. Traeger, Z. Shvets, M. Rojansky, S. Stoyanoff, and J. Garber. Evaluating effects on wind loads in heliostat design. In SolarPACES Conference, Granada, Spain, 2011.

A. Jafari, F. Ghanadi, M. Arjomandi, M. J. Emes, and B. S. Cazzolato. Correlating turbulence intensity and length scale with the unsteady lift force on flat plates in an atmospheric boundary layer flow. Journal of Wind Engineering and Industrial Aerodynamics, 189:218–230, 2019.

R. H. Kraichnan. Diffusion by a random velocity field. The Physics of Fluids, 13(1):22–31, 1970.

T. Lauriks, R. Longo, D. Baetens, M. Derudi, A. Parente, A. Bellemans, J. Van Beeck, and S. Denys. Application of improved cfd modeling for prediction and mitigation of traffic-related air pollution hotspots in a realistic urban street. Atmospheric Environment, 246:118127, 2021.

H. Liu, B. Gong, Z. F. Wanga, and Z. N. Li. Wind tunnel studies of wind fences for reduction of wind flow and wind loads on heliostats. 2014.

R. Longo, P. Nicastro, M. Natalini, P. Schito, R. Mereu, and A. Parente. Impact of urban environment on savonius wind turbine performance: A numerical perspective. Renewable Energy, 156:407–422, 2020.

C. Maliska, E. Paladino, F. Saltara, B. Contessi, R. Ataides, and V. Girardi Silva. A comparison of turbulence models for the computation of a detached flow around a square cylinder. In 20th Annual Conference of the CFD Society of Canada, 2012.

M. D. Marais. Computational fluid dynamics investigation of wind loads on heliostat structures. Master's thesis, University of Pretoria, July 2016.

M. D. Marais, K. J. Craig, and J. P. Meyer. Computational flow optimization of heliostat aspect ratio for wind direction and elevation angle. Energy Procedia, 69:148–157, 2015.

F. Mathey, D. Cokljat, J. P. Bertoglio, and E. Sergent. Assessment of the vortex method for Large Eddy Simulation inlet conditions. Progress in Computational Fluid Dynamics, An International Journal, 6(1-3): 58–67, 2006.

F. R. Menter. Best Practice: Scale-Resolving Simulations in ANSYS CFD. 1:1–70, 2012.

F. R. Menter and Y. Egorov. Revisiting the turbulent scale equation. In IUTAM Symposium on One Hundred Years of Boundary Layer Research, pages 279–290. Springer, 2006.

F. R. Menter and Y. Egorov. The Scale-Adaptive Simulation method for unsteady turbulent flow predictions. Part 1: Theory and model description. Flow, Turbulence and Combustion, 85(1):113–138, 2010.

F. R. Menter, M. Kuntz, and R. Bender. A Scale-Adaptive Simulation model for turbulent flow predictions. In 41st Aerospace Sciences Meeting and Exhibit, 2003.

J. Paetzold, S. Cochard, A. Vassallo, and D. F. Fletcher. Wind engineering analysis of parabolic trough solar collectors: The effects of varying the trough depth. Journal of Wind Engineering & Industrial Aerodynamics, 135:118–128, 2014.

J. Paetzold, S. Cochard, D. F. Fletcher, and A. Vassallo. Wind engineering analysis of parabolic trough collectors to optimise wind loads and heat loss. Energy Procedia, 69:168–177, 2015.

J. Paetzold, S. Cochard, D. F. Fletcher, and A. Vassallo. Wind effects in solar fields with various collector designs. In AIP Conference Proceedings, volume 1734, page 020018. AIP Publishing LLC, 2016.

J. Peterka and R. Derickson. Wind load design methods for ground-based heliostats and parabolic dish collectors. Technical Report SAND92-7009, Sandia National Laboratories, September 1992.

J. Peterka, N. Hosoya, B. Bienkiewicz, and J. Cermak. Wind load reduction for heliostats. Technical Report SERI/STR-253-2859, Colorado State Univ., Fort Collins (USA), May 1986.

J. A. Peterka, B. Bienkiewicz, N. Hosoya, and J. E. Cermak. Heliostat mean wind load reduction. Energy, 12(3):261–267, 1987a. Status of Solar Thermal Research.

J. A. Peterka, L. Tan, B. Bienkiewcz, and J. Cermak. Mean and peak wind load reduction on heliostats. Technical Report SERI/STR-253-3212, Colorado State Univ., Fort Collins (USA), September 1987b.

J. A. Peterka, Z. Tan, B. Bienkiewicz, and J. Cermak. Wind loads on heliostats and parabolic dish collectors: Final subcontract report. Technical Report SERI/STR-253-3431, Solar Energy Research Inst., Golden, CO (USA), November 1988.

J. A. Peterka, Z. Tan, J. E. Cermak, and B. Bienkiewicz. Mean and peak wind loads on heliostats. Journal of Solar Energy Engineering, 111(2):158–164, 1989.

J. A. Peterka, R. G. Derickson, and J. E. Cermak. Wind loads and local pressure distributions on parabolic dish solar collectors. Technical Report SERI/TP-253-3668, Solar Energy Research Inst., Golden, CO (USA), 1990.

A. Pfahl. Survey of heliostat concepts for cost reduction. Journal of Solar Energy Engineering, 136(1), 2014.

A. Pfahl. Wind loads on heliostats and photovoltaic trackers. PhD thesis, Technische Universiteit Eindhoven, 2018.

A. Pfahl, M. Buselmeier, and M. Zaschke. Wind loads on heliostats and photovoltaic trackers of various aspect ratios. Solar Energy, 85(9):2185–2201, 2011a.

A. Pfahl, M. Buselmeier, and M. Zaschke. Determination of wind loads on heliostats. Proceedings SolarPACES 2011 Granada, 2011b.

A. Pfahl, A. Brucks, and C. Holze. Wind load reduction for light-weight heliostats. Energy Procedia, 49: 193–200, 2014.

A. Pfahl, J. Coventry, M. Röger, F. Wolfertstetter, J. Vásquez-Arango, F. Gross, M. Arjomandi, P. Schwarzbözl, M. Geiger, and P. Liedke. Progress in heliostat development. Solar Energy, 152:3–37, 03 2017.

A. S. Pidaparthi. Heliostat cost reduction for power tower plants. PhD thesis, Stellenbosch University, 2017.

S. B. Pope. Turbulent Flows. Cambridge University Press, 2000.

P. E. Poulain, K. J. Craig, and J. P. Meyer. Influence of the gap size on the wind loading on heliostats. In AIP Conference Proceedings, volume 1734. AIP Publishing LLC, 2016a.

P. E. Poulain, M. D. Marais, K. J. Craig, and J. P. Meyer. Using RANS-LES formulations in the CFD modeling of heliostat peak loads. In 4th Southern African Solar Energy Conference, Stellenbosch, South Africa, 2016b.

R. Rebolo, J. Lata, and J. Vazquez. Design of heliostats under extreme and fatigue wind loads. In 17th Annual SolarPACES Symposium, 2011.

P. J. Richards and R. P. Hoxey. Appropiate boundary conditions for computational wind engineering models using the $k-\epsilon$ turbulence model. Journal of Wind Engineering and Industrial Aerodynamics, 46,47:145–153, 08 1993.

J. C. Rotta. Turbulente Strömungen. Teubner Verlag, 1972.

E. Sergent. Vers une methodologie de couplage entre la Simulation des Grandes Echelles et les modeles statistiques. PhD thesis, Ecole centrale de Lyon, Ecully, France, 2002.

E. Simiu and R. H. Scanlan. Wind effects on structures: Fundamentals and application to design, volume 605. Wiley, 1996.

J. Sment and C. K. Ho. Wind patterns over a heliostat field. Energy Procedia, 49:229–238, 2014. Proceedings of the SolarPACES 2013 International Conference.

A. Smirnov, S. Shi, and I. Celik. Random flow generation technique for Large Eddy Simulations and particle-dynamics modeling. J. Fluids Eng., 123(2):359–371, 2001.

ANSYS. ANSYS Fluent Theory Guide, release 2019 R3. ANSYS Inc., Canonsburg, PA, 2019.

IRENA. Renewable energy technologies: Cost analysis series. Volume 1: Power sector, June 2012.

IRENA. The power to change: Solar and wind cost reduction potential to 2025. June 2016.

IRENA. Renewable power generation costs in 2019. 2020.

I. Van der Hoven. Power spectrum of horizontal wind speed in the frequency range from 0.0007 to 900 cycles per hour. Journal of Meteorology, 14(2):160–164, 1957.

J. F. Vásquez-Arango, R. Buck, and R. Pitz-Paal. Dynamic properties of a heliostat structure determined by numerical and experimental modal analysis. Journal of Solar Energy Engineering, 137(5), 2015.

J. F. Vásquez-Arango, R. Pitz-Paal, and M. Breuer. Dynamic wind loads on heliostats. PhD thesis, 2017.

J. R. Wolmarans and K. J. Craig. One-way fluid-structure interaction of a medium-sized heliostat using scale-resolving CFD simulation. Solar Energy, 191:84–99, 2019.

Z. Wu, B. Gong, Z. Wang, Z. Li, and C. Zang. An experimental and numerical study of the gap effect on wind load on heliostat. Renewable Energy, 35(4):797–806, 2010.

C. Zang, Z. Wang, H. Liu, and Y. Ruan. Experimental wind load model for heliostats. Applied energy, 93:444–448, 2012.

M. K. Zemler, G. Bohl, O. Rios, and S. K. Boetcher. Numerical study of wind forces on parabolic solar collectors. Renewable Energy, 60:498–505, 2013.

J. Zhang, H. Meng, B. Gu, and P. Li. Research on short-term wind power combined forecasting and its gaussian cloud uncertainty to support the integration of renewables and evs. Renewable Energy, 153:884–899, 2020.

W. Zheng, C. Yan, H. Liu, and D. Luo. Comparative assessment of SAS and DES turbulence modeling for massively separated flows. Acta Mechanica Sinica, 32(1):12–21, 2016.